ISSN (Print) 1226-1750
ISSN (Online) 2233-6656
Journal of Magnetics 26(1), 87-100 (2021) https://doi.org/10.4283/JMAG.2021.26.1.087

The Balanced Method of Magnetic Torque Under Wind Load for HVDC Inspection Robot

Xianjin Xu[1]*, Yuhang Yang[1], Haoda Chen[1], Lanlan Liu[2], and Yu Yan[2]

[1]Hubei University of Technology, College of Mechanical Engineering, Hubei Wuhan, 430068, China
[2]State Grid Hunan Electric Power Company Live Line Inspection and Intelligent Work Technology State Grid Corporation Laboratory, Hunan Changsha, 410004, China

(Received 18 October 2020, Received in final form 9 February 2021, Accepted 17 February 2021)

Aiming at the problem that the high-voltage inspection robot is susceptible to wind load when inspecting the line, which leads to poor stability and low safety of the airframe, a balanced method of magnetic torque based on HVDC magnetic field is proposed: The dynamic balance is achieved through the ampere torque which is generated by the current-carrying coil in the HVDC magnetic field to offset the wind load moment. According to the actual working conditions of the inspection robot, a magnetic torque simulation model which was calculated and simulated was established. The results show that the model could produce a magnetic torque which met the requirements under the set parameters. Finally, an experiment was conducted on the magnetic torque device which showed that the torque generated by the device was sufficient to meet the requirements in non-extreme wind speed environments. In addition, the method used the magnetic torque to offset the wind load moment, which provided an effective idea for facing more complex load situations.

Keywords : inspection robot, wind load, magnetic torque, balance control

1. Introduction

The safe and stable operation of the power system is an important guarantee for the normal operation of society. The power distribution process is easily affected by natural and man-made factors, causing failures of the fittings and wires on the line. Therefore, the daily inspection and maintenance of the transmission line is particularly important. Since high-voltage transmission lines are generally erected in open areas with sparsely populated, inspection robots are prone to frequent wind impacts during work. As a result, when the robot is working online, the stability of the airframe is poor, the inspection quality is low, and the safety of the operation couldn't be guaranteed. Reference [1] analyzed the influence of the size of the robot structure on its wind load, and redesigned and optimized the size parameters; Reference [2] proposed a method for posture detection and job optimization of inspection robots under wind load, but it did not fundamentally solve the influence of wind load.

With the increasing demand for robots to inspect high-voltage and ultra-high-voltage transmission lines in the power sector of various countries, some countries have successively carried out research on high-voltage line inspection robots. For example, the "LineScout" inspection robot of the Quebec Hydropower Research Institute in Canada [3-9], and the "Expliner" inspection robot developed by the Japanese "HiBot" company Paulo Debenest and others [10]. The revolving two-arm inspection robot that walks on grounding wire was developed by the Shenyang Institute of Automation, Chinese Academy of Sciences [11-14]. Since 2015, Fan Shaosheng of Changsha University of Science and technology and State Grid Hunan electric power company have cooperated to develop a variety of live working robots for transmission lines for repairing broken stocks, tightening bolts, and replacing shock-proof hammers [15-18]. Because the robots which was mentioned in the above references have not been improved for the influence of wind load, they all have the problem of poor wind load resistance.

This paper proposes a balanced method of magnetic torque. In order to make the HVDC inspection robot maintain a stable posture in high-altitude operations, a magnetic force model was established to balance the wind

*Corresponding author: Tel: +86 02759750418
Fax: +86 02759750418, e-mail: xxjoyjn@126.com

load moment; When the airframe tilts, the coil current of the magnetic torque device was controlled to generate a magnetic torque which was equal to the wind load moment and acts opposite to the wind load moment to maintain the airframe in a balanced and stable state with eliminating the problems of skid and wear of the robot under wind load.

2. The Balanced Theory of Magnetic Torque

2.1. Analysis of magnetic field characteristics of HVDC transmission lines

At present, the overhead HVDC lines operating on the grid adopt the transmission mode of multiple circuit transmission line and bipolar system which could effectively improve the transmission capacity of unit line corridor. It is also suitable for transmission with different transmission directions or different voltage levels using the same channel locally when the line channel is tight. Take it as an example to analyze its magnetic field characteristics.

The line section was taken as shown in Fig. 1 as an example. In the Fig. 1, the distance between the two high-voltage line B and C is S, and the distance between the two high-voltage line C and D is H. In domestic ± 800 kV double-circuit and bipolar system transmission line, $S = 22$ m [19], $H = 15$ m. It is assuming that a point O was taken at any position of the circle which the radius was d_0 with the high voltage line A as the center. The vertical angle between point O and high-voltage line A was β. The vertical angle between point O and high-voltage line B was α. In the Fig. 1, B_a, B_b, B_c and B_d were the magnetic induction intensity of high voltage line A, B, C and D at point O. B_{ab} was the combined magnetic field strength of high voltage line A and B at point O.

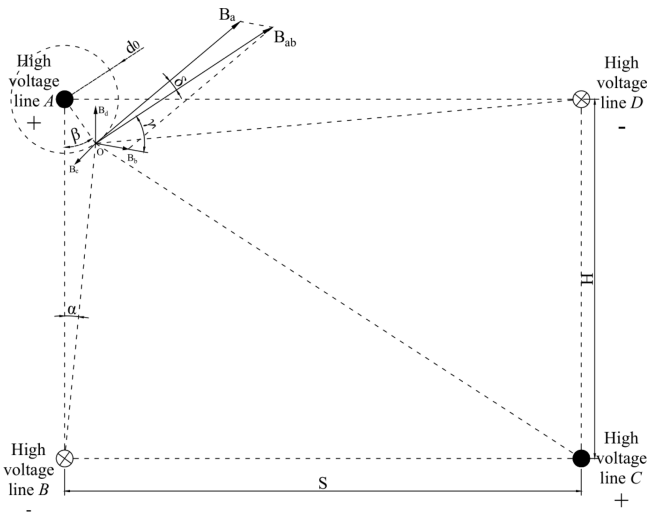

Fig. 1. Bipole line with magnetic field analysis.

Firstly, according to the Biot-Savart Law, the magnetic induction intensity B_a and B_b were perpendicular to OA and OB respectively, it could be obtained

$$B_a = \frac{\mu_0 I_A}{2\pi L_{OA}} \tag{1}$$

$$B_b = \frac{\mu_0 I_B}{2\pi L_{OB}} \tag{2}$$

μ_0 is permeability of vacuum ($\mu_0 = 4\pi \times 10^{-7}$ H/m). From the geometric relationship, $\Delta OAB \backsim \Delta B_a B_b B_{ab}$, it could be derived as

$$\angle\alpha = \angle\delta, \angle\beta = \angle\gamma \tag{3}$$

$$\frac{B_a}{L_{OB}} = \frac{B_b}{L_{OA}} = \frac{B_{ab}}{H} \tag{4}$$

By the Law of Cosines, it could be obtained

$$COS\beta = \frac{H^2 + L_{OA}^2 - L_{ob}^2}{2HL_{OA}} \tag{5}$$

The calculated magnetic induction intensity B_{ab} was

$$B_{ab} = \frac{\mu_0 I_A H}{2\pi L_{OA} L_{OB}} = \frac{\mu_0 I_A H}{2\pi L_{OA}\sqrt{H^2 + L_{OA}^2 - 2HL_{OA}COS\beta}} \tag{6}$$

According to equation (1) to (6), the ratio of magnetic induction B_a to combined magnetic induction B_{ab} was K_1,

$$K_1 = \frac{B_{ab}}{B_a} = \frac{H}{L_{OB}} = \frac{H}{\sqrt{H^2 + L_{OA}^2 - 2HL_{OA}COS\beta}} \tag{7}$$

According to the size of the designed inspection robot, the farthest distance between the current-carrying coil and the high-voltage line was 0.08 m after the magnetic device was installed in the robot, $L_{OA} = d_0 = 0.08$ m. From formula (7), the value range of K_1 was obtained:

$$K_1 \in [0.995, 1.005]$$

It could be seen from the value range of K_1 that the interference of B_b to B_a was very small; In the same way, the influence of magnetic field produced by the wires C and D on B_a was calculated as follows: $K_2 \in [0.996, 1.004]$, $K_3 \in [0.997, 1.003]$. Adding the left and right maximum values of K_1, K_2 and K_3, the value range $K \in [0.988, 1.102]$ was obtained. Therefore, when the influence of B, C and D on A at point O was the maximum value, the interference to B_a was also very small. Therefore, in the subsequent magnetic field analysis, the magnetic field around a single wire is considered as a steady-state ring-shaped magnetic field.

2.2. Design of magnetic torque model

At present, most of the inspection robots which was developed at home and abroad adopt wheel arm structure, which leads to poor wind load resistance of inspection robots. The structure of inspection robot [20-22] is shown in Fig. 2.

The two sides of the current-carrying coil which was embedded in the magnetic core were called the force side, and the two sides in the air were called the invalid side; As shown in Fig. 3, in order to ensure the operation quality of inspection robot under wind load and improve its stability and safety, a magnetic core made of soft magnetic material was designed. The magnetic torque by the force side in this strengthened magnetic field was

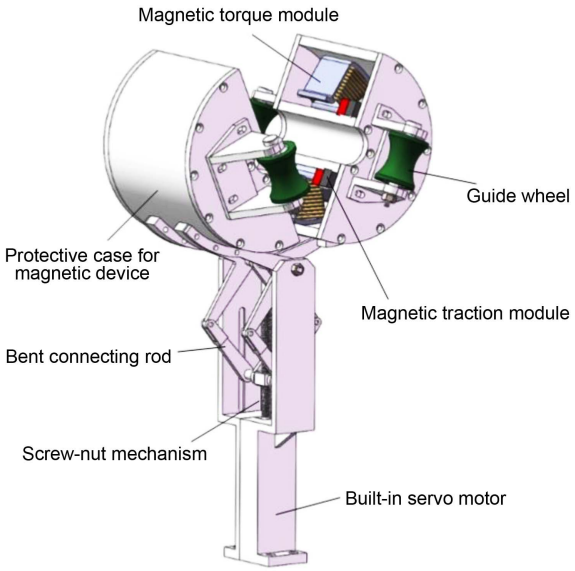

Fig. 2. (Color online) Overall structure of inspection robot.

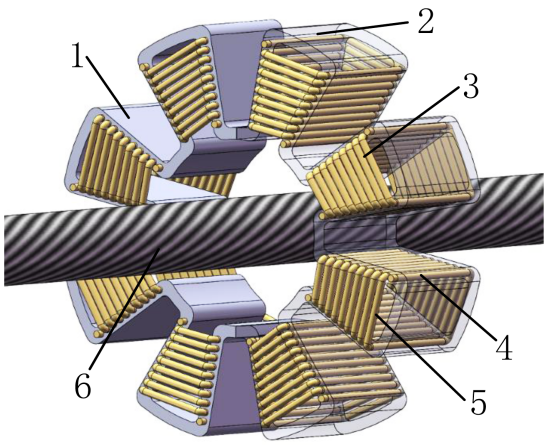

Fig. 3. (Color online) Magnetic torque model: 1-left, 2-right, 3-Current-carrying coil, 4-Force side, 5-Invalid side, 6-High-voltage line

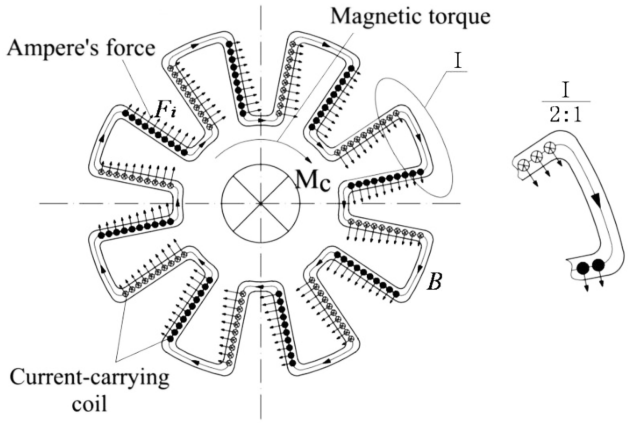

Fig. 4. Force on the magnetic torque model.

enough to overcome the influence of the cross wind moment at a certain wind speed due to the characteristics of magnetic flux concentration of soft magnetic materials. Due to the low magnetic flux density in air, the ampere force on the invalid side could be ignored. The direction and magnitude of the torque were determined by the direction and magnitude of the current in the coil. As shown in Fig. 4 (× and • mean the direction of the current).

According to Ampere's law, the ampere force experienced by the i-th current-carrying coil on any boss was:

$$F_i = 2BI_0L\sin\theta_1 \tag{8}$$

Due to the characteristics of soft magnetic materials, the magnetic field strength of the current-carrying coil which was inserted in the guide hole was greatly increased:

$$B = \frac{\mu_r\mu_0 I_1}{2\pi R_i} \tag{9}$$

The current direction in the current carrying coil was perpendicular to the internal magnetic field of the magnetic core, $\theta_1 = 90°$. Formula (8) was simplified:

$$F_i = \frac{\mu_r\mu_0 I_0 I_1 L}{\pi R_i} \tag{10}$$

In formula (10), I_0 is the coil current, I_1 is the high voltage line current, and L is the length of the magnetic torque model. R_i is the distance from the forced side of the i-th current carrying coil on the boss to the high voltage line. The magnetic torque produced by the coil was:

$$M_i = F_i \times R_i = \frac{\mu_r\mu_0 I_0 I_1 L}{\pi} \tag{11}$$

From formula (11), it could be seen that the moment produced by the force side of each current-carrying coil was the same. The invalid side was placed in the air and

would not be discussed.

Assuming that the number of bosses was m and the number of turns on each boss was n. Then the torque on the magnetic torque model was:

$$M_c = \sum_{i=1}^{n} mM_i = mn\frac{\mu_r\mu_0 I_0 I_1 L}{\pi} \tag{12}$$

The number of boss is m which related to the value of the included angle α_1. In order to ensure bilateral symmetry of the model, the value of m was an even number. The value of m decreases with the increase of α_1 ($\alpha_1 > 0$):

$$m = \frac{2\pi}{2\alpha_1} = \frac{\pi}{\alpha_1} \tag{13}$$

The number of coils on the boss is n which related to the maximum outer diameter of the actual magnetic torque model. Therefore, it was necessary to choose different sizes of magnetic torque devices according to the actual situation. The extreme value of the model outer diameter was R_1, and maximum number of coils arranged on a single boss was $n_{\max}$:

$$n_{\max} = \left\lfloor \frac{R_1 - R_0 - 2d}{l} \right\rfloor + 1 \tag{14}$$

The number of boss m and the number of single boss coil $n_{\max}$ should be rounded.

To sum up, under ideal conditions, the magnetic torque provided by the model was directly proportional to the number of boss, number of current carrying coils, high voltage line current, coil current, model thickness and relative permeability of soft magnetic materials.

3. Calculation and Simulation Analysis of Wind Load

3.1. Force analysis of robot under wind load

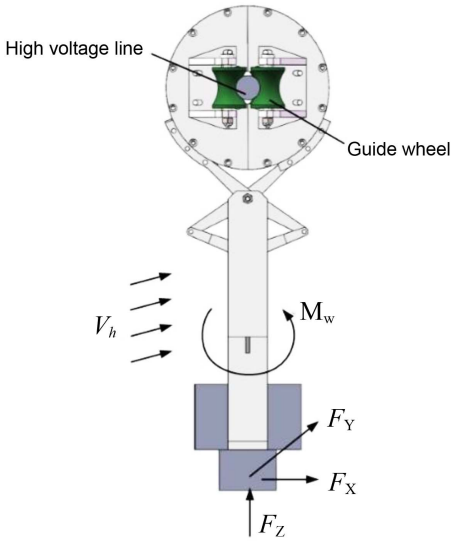

Fig. 5. (Color online) Force analysis of robot.

Since the inspection robot is frequently subjected to wind loads during operation, analyzing the impact of wind load on the inspection robot during operation is of practical significance for improving the quality, efficiency and safety of the inspection operation. Therefore, combined with the operating environment of the inspection robot on the overhead transmission line, the force diagram of the robot as shown in Fig. 5 was established. Under the wind load, the wind force on the robot could be divided into three directions: Cross Wind F_X, the component of parallel to line direction F_Y, Vertical component F_Z.

Given that the total mass of the robot was 27 kg. Without considering the extreme wind speed, the vertical component force (F_Z << mg) caused by the wind load under general wind speed conditions has little effect on the position of the robot. Therefore, the cross wind force F_X had the greatest impact on the stability and operation

Table 1. Nonuniform coefficient of wind speed α.

Wind speed V (m/s)	$V < 20$	$20 \le V < 30$	$30 \le V < 35$	$V \ge 35$
Nonuniform coefficient of wind speed α	1.0	0.85	0.75	0.70

Table 2. wind speed amplification K_h.

Height h (m)	10	20	30	40	50	60	70	80	90
Wind speed amplification K_h	1.0	1.12	1.19	1.24	1.28	1.31	1.34	1.38	1.40

Table 3. aerodynamic coefficient K ($\theta_2 = 90°$).

Line diameter D (mm)	$D < 17.0$	$D \ge 17.0$	Icing (Regardless of diameter)
Aerodynamic coefficient K	1.2	1.1	1.2

safety of the inspection robot. The calculation formula of cross wind force F_X was as follows:

$$F_x = \frac{1}{2}\alpha\rho KSK_h^2 v_0^2 \sin^2\theta_2 \quad (15)$$

ρ is air density (1.225 kg/m^3); α is nonuniform coefficient of wind speed, shown in Table 1; K_h is wind speed amplification, shown in Table 2; K is aerodynamic coefficient, shown in Table 3; The projected area of the wind is A m^2. The wind speed is V m/s.

3.2. Establishing a simulation model

Based on ANSYS-Workbench software, in order to facilitate the analysis, the inspection robot was simplified reasonably. The simplified simulation model of the inspection robot was shown in Fig. 6(a). The overall dimensions were 0.92 m in length, 0.20 m in width and 0.59 m in height. In order to meet the requirements of numerical simulation calculations, a fluid domain of regular dodecahedron prism of wrapping robot model was established. The fluid domain requires a blocking ratio of less than 3 %. The inscribed circle radius of the dodecahedral prism fluid domain was 60 m and the height was 60 m, as shown in Fig. 6(b). Realize the calculation of the wind moment of the robot under different wind direction angles by changing the inlet and outlet faces of different wind fields. The wind angle perpendicular to the robot running direction was defined as 90° ($\theta_2 = 90°$).

In wind load analysis, the model was imported into CFX to suppress the solid model. The flow field was divided into two computational domains. The outer domain was divided into hexahedral mesh and the inner domain was divided into tetrahedral mesh. The expansion transition layer was set at the junction of the inner and outer grids; In static structure analysis, the model was imported into the Static Structure module to suppress the flow field. The

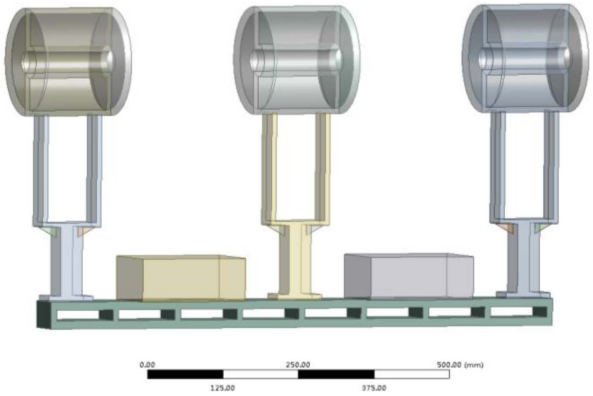

(a) Simplified model of inspection robot

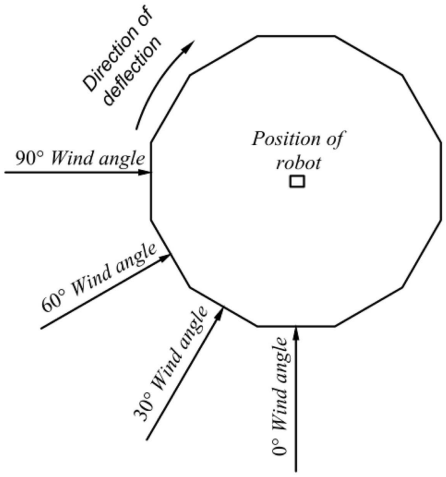

(b) Fluid domain model

Fig. 6. (Color online) Simulation model.

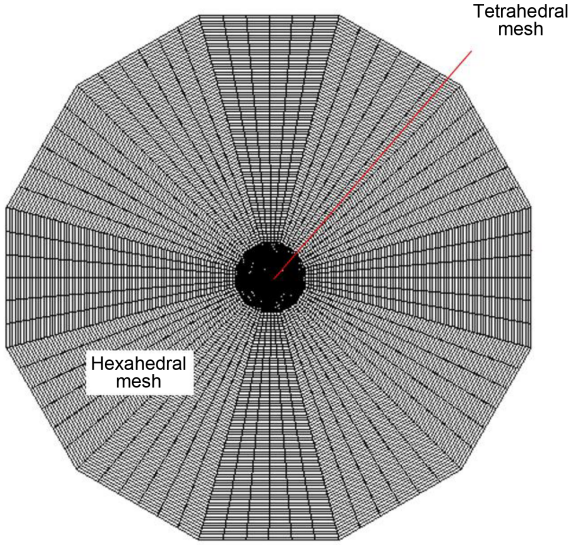

(a) fluid domain meshing

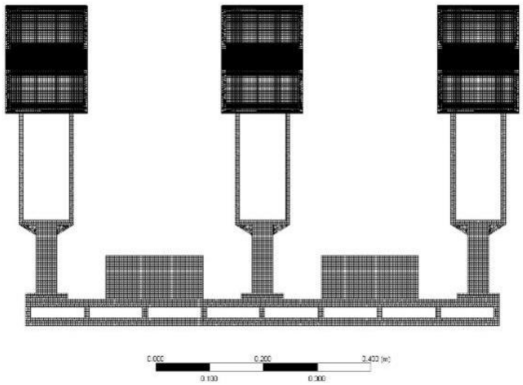

(b) Solid domain meshing

Fig. 7. (Color online) Model meshing.

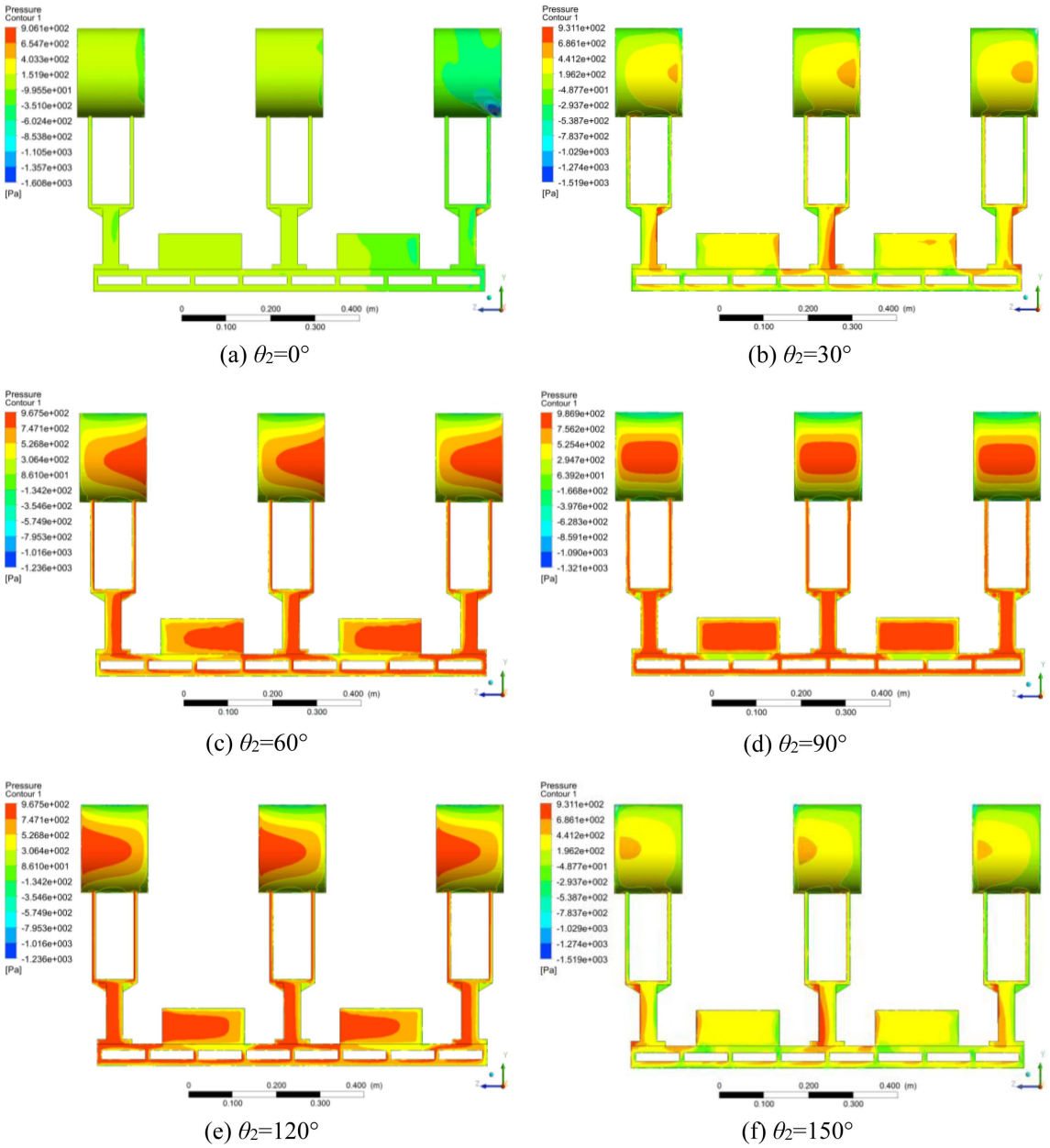

Fig. 8. (Color online) Pressure nephogram of robot.

solid model was divided by hexahedral mesh, and the model mesh was shown in Fig. 7. After meshing, the number of nodes in the flow field was 1515602 and the number of elements was 5078256. In the solid domain, there were 2136580 nodes and 456633 elements. The mesh quality met the requirements.

3.3. Simulation analysis

In CFX solver, no heat conduction and *k-epsilon* model were selected to solve the steady-state problem. The choice of medium is incompressible 25 ℃ air. The entrance boundary type was defined as Inlet, and the entrance speed was set to 31.95 m/s; The export boundary type was defined as Outlet. The relative atmospheric pressure was set to 0 MPa; The internal and external interface was set to Interface. The rest of the surfaces and robot surfaces were set as non-slip wall type (Wall). The solution of robot pressure nephograms was shown in Fig. 8.

Through the Fig. 8, when the wind direction angle was $0° \leq \theta_2 < 90°$, the wind area and surface wind pressure of the airframe gradually increase with the wind direction angle gradually increases; when the wind direction angle was $90° \leq \theta_2 < 150°$, the wind area and surface wind pressure of the airframe gradually decrease with the wind

Table 4. The maximum wind moment of the robot under different wind directions (Method of fluid-structure interaction).

Wind direction θ_2	0°	30°	60°	90°	120°	150°	180°
Wind moment M_s (N·m)	1.81	7.30	18.37	24.46	18.34	7.28	1.81

Table 5. Cross wind force on the robot under different wind directions.

Wind angle θ_2	0°	30°	60°	90°	120°	150°	180°
Cross wind force F_X (N)	0	37.45	112.34	149.79	112.34	37.45	0

Table 6. The maximum wind moment of the robot under different wind directions (Method of calculations).

Wind angle θ_2	0°	30°	60°	90°	120°	150°	180°
Wind moment M_s (N·m)	0	6.53	19.66	26.22	19.66	6.53	0

direction angle continues to increase; Among them, when the wind direction angle was θ_2 ($\theta_2 = 90°$), the wind area and surface wind pressure reach the peak value.

In the static analysis of the structure, the main airframe was made of aluminum alloy, the material density was 2270 kg/m^3, the Young's modulus was 75 GPa and the Poisson's ratio was 0.33; For the control box, its material density was defined as 1068 kg/m^3, and Poisson's ratio was 0.28. The load was applied on the coupling surface (the surface facing the 90° wind direction angle), and the inner wall of the protective sleeve of the magnetic device was fixed with a gravity acceleration of 9.806 m/s^2 and the direction was vertical downward. The maximum wind moment of the robot under different wind directions was shown in Table 4.

In order to verify the correctness of the method of fluid-structure interaction, the cross wind force F_X on the robot was taken as the wind pressure to calculate the torque on the robot. v_0 was the minimum design wind speed of HVDC transmission line ($v_0 = 26.85$ m/s). Nonuniform coefficient of wind speed α was 0.85; Wind speed amplification K_h was 1.19; High-altitude wind velocity v_h was 31.95 m/s; aerodynamic coefficient K was 1.2; Wind area of robot model S was 0.243 m^2. The cross wind force F_X was solved by formula (15), as shown in Table 5.

The torque M_W of the model was solved by the value in Table 5, and results were shown in Table 6.

The values of wind moment which was obtained by the two methods were compared, as shown in Fig. 9.

It could be clearly seen from the Fig. 9 that the results of fluid-structure interaction was large due to the flows around bluff bodies by non-streamlined shape when the wind direction angle was small; With the increase of wind direction angle, the flows around bluff bodies was weakened, and the simulation results were slightly larger. The reason for the error was that the model simplification process was not completely equivalent to simplification, resulting in reduced wind area. But the error between the two methods was small, which verifies the correctness of the method of fluid-structure interaction to solve the wind moment.

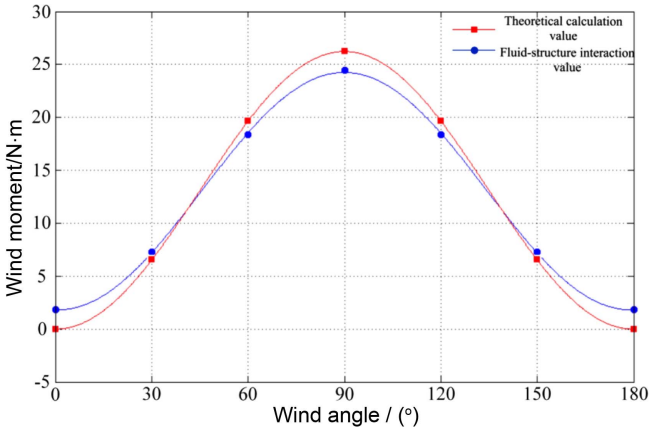

Fig. 9. (Color online) Comparison of wind moment values between two methods.

4. Simulation Analysis of Magnetic Torque

4.1. Building a finite element simulation model

In order to verify the correctness of the theoretical analysis of the magnetic torque device model, the parameters were instantiated. High voltage line current I_1 = 1000 A; High voltage line section ($0.015 \times 0.015\pi$) m^2; Inner diameter $R_0 = 0.03$ m; Maximum outer diameter R_2 = 0.09 m; Model thickness $d = 0.006$ m; Model length L = 0.09 m; Coil guide hole diameter $d_1 = 0.003$ m; Spacing l = 0.0045 m; Coil current $I_0 = 10$ A; All the parameters were brought into formula (14) to find the maximum number ($n_{max} = 12$) of coils on a single boss. The soft magnetic material used in magnetic drive was MnZn

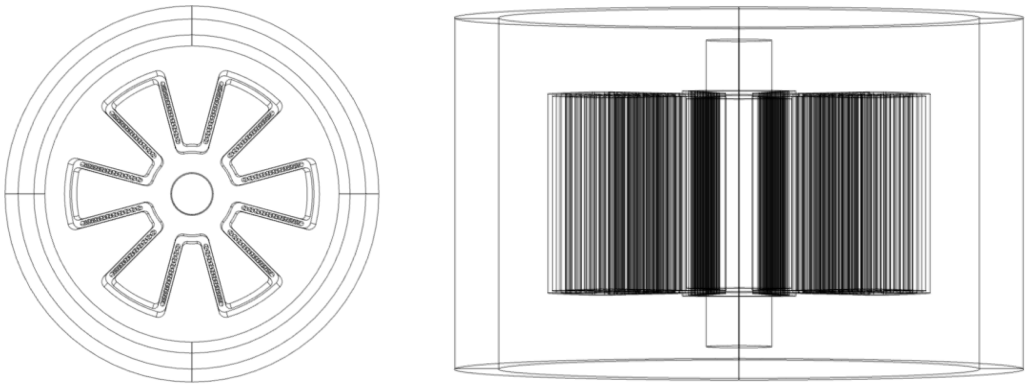

(a) *xy* plane (b) *xz* plane

Fig. 10. Simulation model of magnetic torque ($\alpha_1 = 30^\circ$).

ferrite which relative permeability was as high as 3000 H/m. Considering the economic problem, $\mu_r = 1000$ H/m was proposed.

In order to facilitate simulation analysis, the entity model was simplified. Taking the coil turns $n = 10$ and the included angle $\alpha_1 = 22.5°$, 30°, 45°, 90° to establish the simulation model, as shown in Fig. 10.

4.2. Simulation analysis

Simulation 1 The influence of the number of bosses on the magnetic torque

The COMSOL software was used for simulation analysis. The physical field was selected as a magnetic field, and the material properties of the magnetic torque device model were set; The number of bosses m was selected as 2, 4, 6, 8 respectively, and the number of coils n was 10. The free tetrahedral grid ultra-fine mesh method was used for the magnetic core, current-carrying coil, high voltage line and inner air domain, while the free tetrahedral grid finer mesh method was used for other outer air domain. A steady-state magnetic field environment was generated by high voltage current (1000A), and the model was calculated by the FGMRES. The Fig. 11 was the interface magnetic flux density model (six bosses), and Fig. 12 was the surface magnetic field mode and surface arrow of the model.

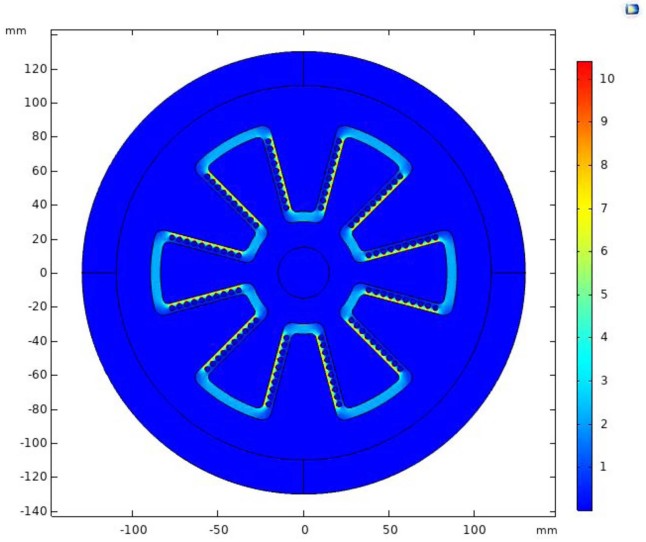

Fig. 11. (Color online) Magnetic flux density mode.

It could be seen from Fig. 11 that the soft magnetic material could obviously enhance the magnetic field, and the magnetic field of the high-voltage line was coupled with the magnetic field of the coil; In Fig. 12, the direction of the arrow was the direction of the magnetic induction within the model. The density of the surface arrow represents the density of the magnetic flux density. It was observed from the Fig. 12 that the original circular magnetic field of the high-voltage line became a curved magnetic field which was surrounding the outer structure of the magnetic core. And the surface arrows were denser at the corner of the bottom of the boss, so the more the boss is, the greater the field strength is, and the greater the magnetic torque is. However, too many bumps will make the magnetic torque too large, which makes it impossible to balance the wind torque.

The finite element method based on the variational principle was used to solve the ampere force:

Table 7. Simulation value of magnetic torque.

Number of model bosses m	M_x (N·m)	M_y (N·m)	M_z (N·m)
2	8.658×10^{-3}	-7.137×10^{-4}	6.649
4	6.255×10^{-3}	-2.232×10^{-5}	13.023
6	6.357×10^{-4}	-2.527×10^{-5}	19.594
8	9.194×10^{-4}	-2.678×10^{-5}	26.198

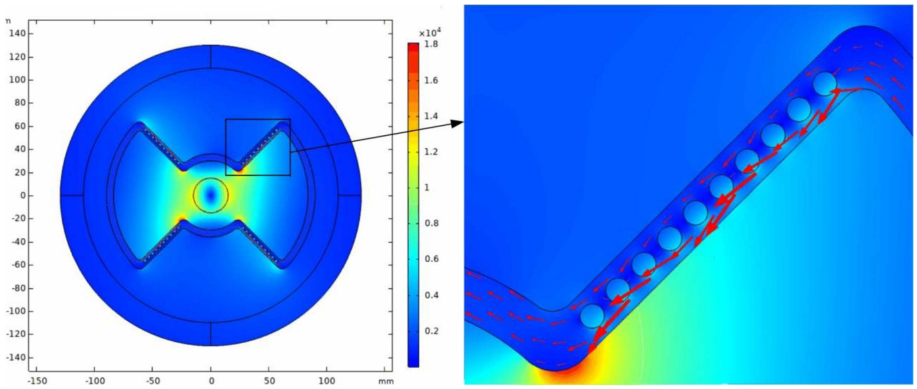

(a) m=2，n=10

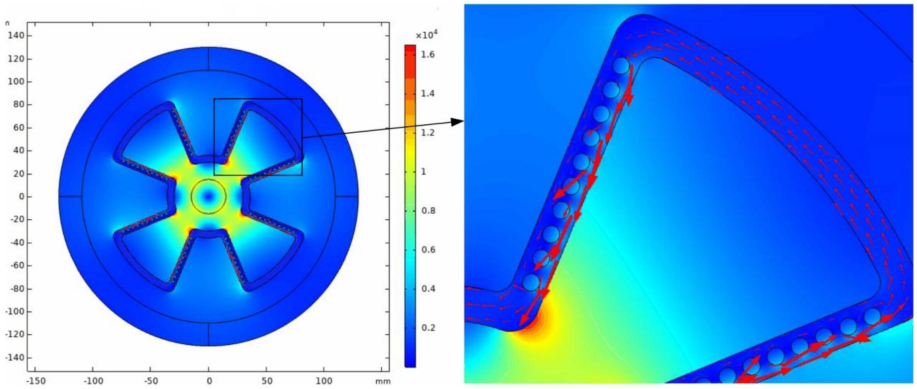

(b) m=4，n=10

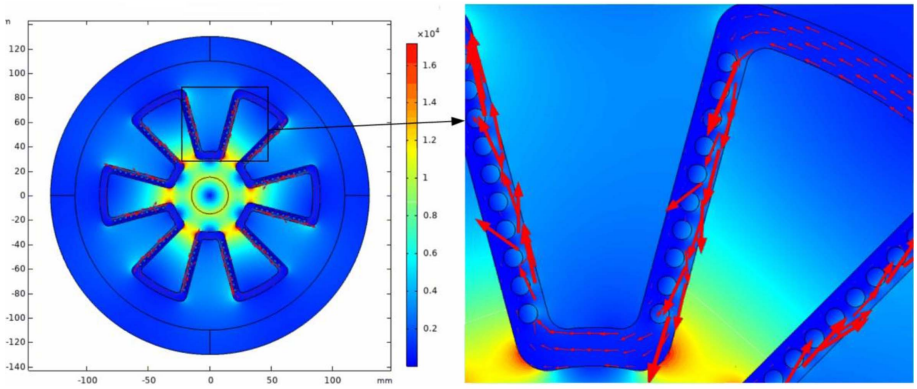

(c) m=6，n=10

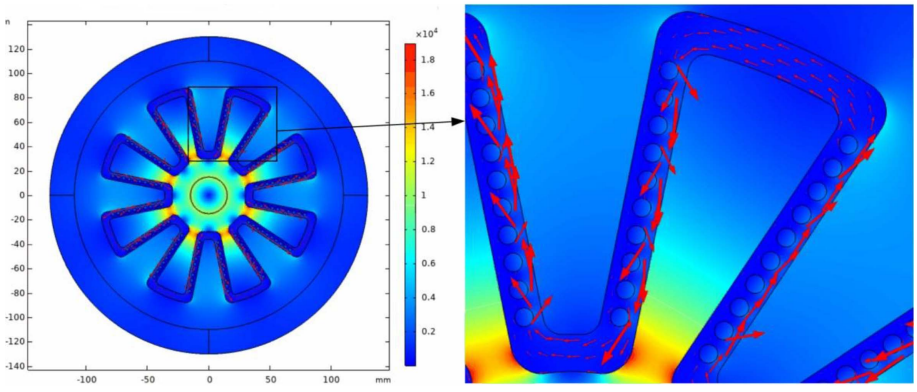

(d) m=8，n=10

Fig. 12. (Color online) The surface magnetic field mode and surface arrow.

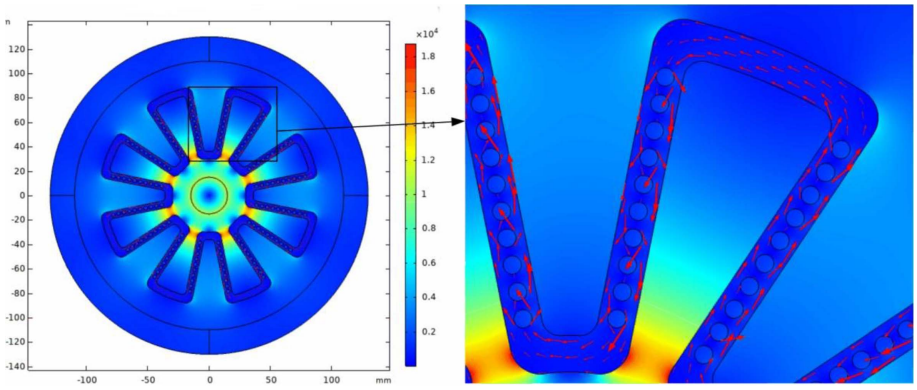

(a) I_0=2

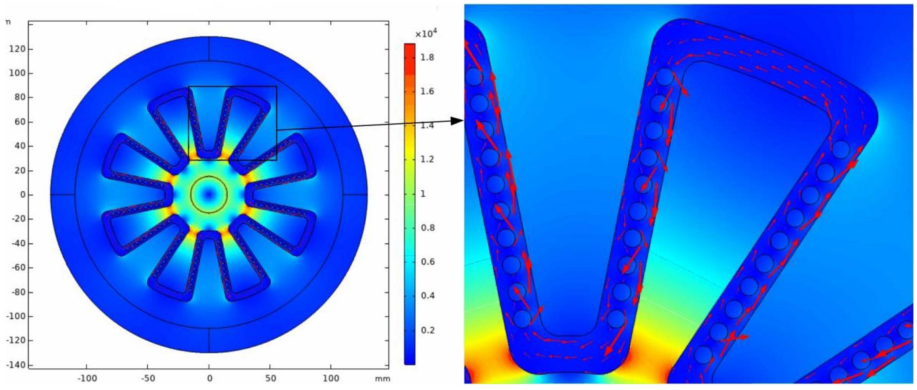

(b) I_0=4

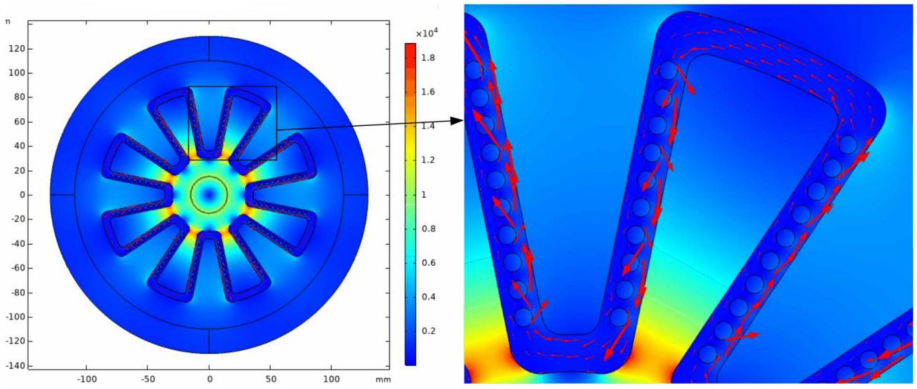

(c) I_0=6

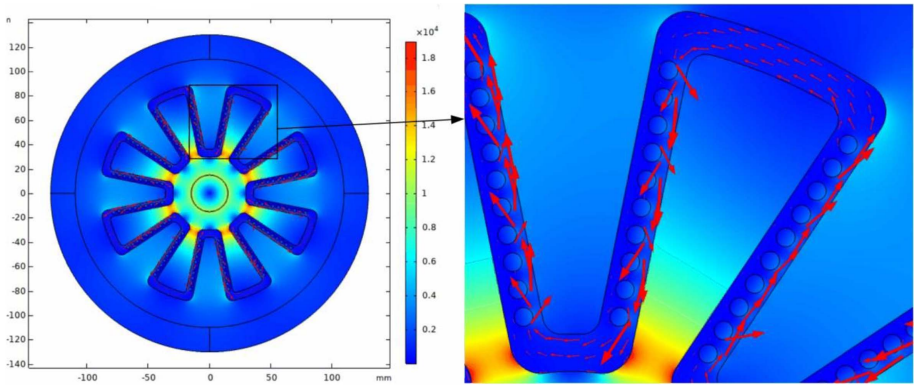

(d) I_0=8

Fig. 13. (Color online) Simulation section of different coil turns.

$$F = \int_{\partial\Omega} nTds \tag{16}$$

T is Maxwell stress tensor [23]; The components of the magnetic torque in the x, y, and z directions were shown in Table 7.

The theoretical torque by formula (12) by the magnetic torque model with the number of bosses 2, 4, 6, 8 were 7.2 N·m, 14.4 N·m, 21.6 N·m, 28.8 N·m. It could be seen that the error between the simulation value and the theoretical value was small, and the torque generated by the 8 bosses was enough to balance the wind torque, which verifies the correctness of the magnetic torque model.

Simulation 2 The influence of coil current on magnetic torque

Considering that the terrain had a great influence on the wind speed near the ground, the robot bears a relatively large wind pressure in a short time. Therefore, it is necessary to analyze the influence of coil current on torque generation. The mesh adopted a division method of extreme refinement for free triangulation. Based on the model of 8 bosses, it was solved under the conditions of coil current I_0 = 2, 4, 6, 8 A; The xy cross section of the simulation model was shown in Fig. 13.

Table 8. Axial torque of different coil current models in z-axis.

Coil current I_0	2	4	6	8	10
M_z (N·m)	5.241	10.483	15.712	20.954	26.198
M (N·m)	5.76	11.52	17.28	23.04	28.8
ΔM	0.519	1.037	1.568	2.086	2.602

It could be seen from Fig. 13 that the coupling between the coil magnetic field and the high-voltage magnetic field inside the model became more serious with the increase of coil current in the same high-voltage magnetic field environment.

Through the comparison between the simulation value

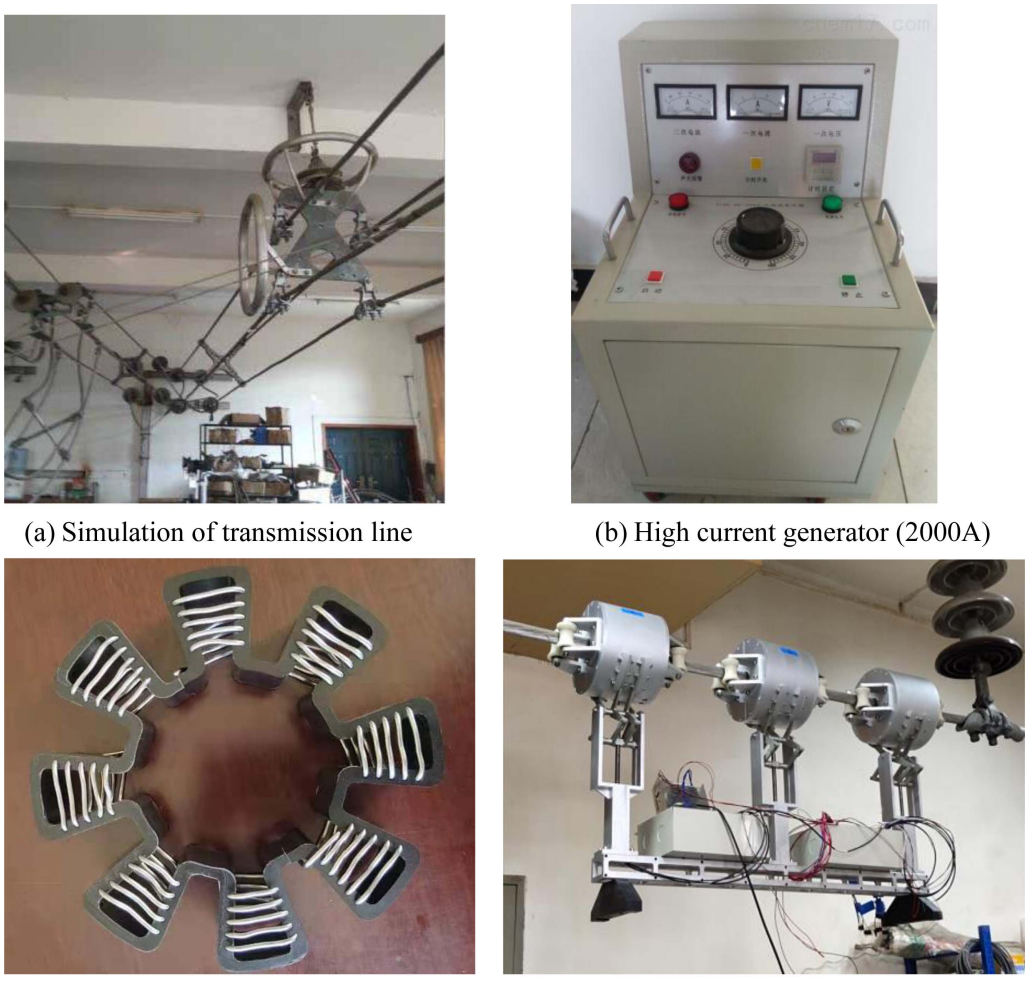

(a) Simulation of transmission line (b) High current generator (2000A)

(c) Magnetic torque device (d) Prototype platform

Fig. 14. (Color online) Experimental equipment.

and the theoretical value, the larger the coil current would cause more serious magnetic field coupling under the same high voltage line magnetic field environment. The study of its variation law was helpful to improve the reliability of magnetic torque device and adapt to more complex transmission line environment. On the contrary, it guides the optimization and improvement of the balanced method of magnetic torque.

5. Experiment

According to the parameters of the simulation model, the magnetic torque device was made. The charged experiment was carried out on the magnetic torque device. The experimental equipment were high current generator (2000 A), digital tension meter (range 0-500N), inclination sensor, magnetic torque device, inspection robot and a simulated high-voltage transmission line. Because the actual processing size of the boss had been reduced by half, each boss had only five pairs of coil guide holes. The 5-turn coil wound on a single boss does not meet the experimental requirements. In the experiment, multiple groups of the same devices were cascaded to simulate the 10-turn coil. The current source provides 10A current to the coil, and the current generator provides 1000A current to the high-voltage line. The maximum outer diameter of the device was R_1 (R_1 = 0.065 m); The minimum inner diameter was R_0 (R_0 = 0.03 m); The soft magnetic material was MnZn ferrite. In order to prevent magnetic leakage, the coil was made of soft iron, and epoxy resin mixed with manganese-zinc ferrite magnetic powder was injected into the gap between the coil and the magnetic core. As shown in Fig. 14.

Experiment 1: Comparison of experimental and theoretical values of different boss number devices

The magnetic torque devices with 2, 4, 6, 8 bosses were installed in the protective sleeve of the magnetic device of the power manipulator, and the charged experiment was carried out on the simulated high voltage transmission line. The magnetic torque produced by the device was measured when the coil turns were 10, the coil current was 10 A and the high voltage line current was 1000 A. The results were shown in Fig. 15.

Experiment 2: Comparison of experimental measurement value, theoretical calculation value and simulation analysis value of 8 bosses device under different coil current

Taking 8 bosses device as the experimental object, the coil current of 2, 4, 6, 8, 10 A was supplied by changing the DC power supply under the condition of constant high voltage line current. The magnetic torque generated by the device was measured, and the measured results were compared with the theoretical calculation value and simulation analysis value, as shown in Fig. 16.

Comparing the two groups of experimental data, it could be seen that the magnetic torque device could produce the torque which made the robot deflect. The torque direction was the same as the theoretical direction, but the actual measured value was small. There was a certain error between the magnetic torque device and the theoretical calculation value and the simulation analysis value. The error between the experimental measured value and the theoretical data gradually increases with the increase of the number of boss in Fig. 15. The main reason was that a gap between the magnetic core and the coil in the coil guide hole, and the magnetic force in the magnetic core was not closed causing magnetic flux leakage. Although the epoxy resin mixed with ferrite powder was injected into the gap at medium pressure before the experiment, the magnetic flux leakage still

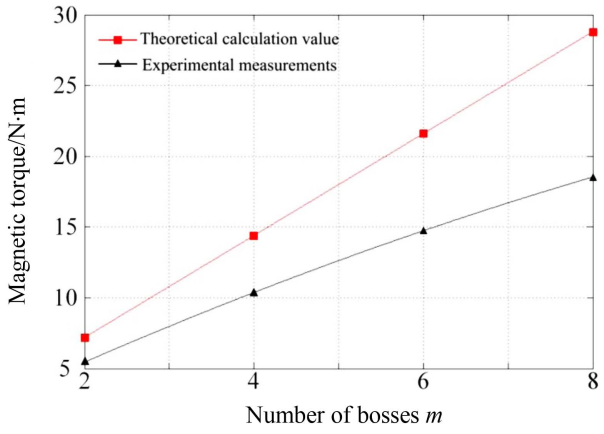

Fig. 15. (Color online) Comparison of Experiment 1 data.

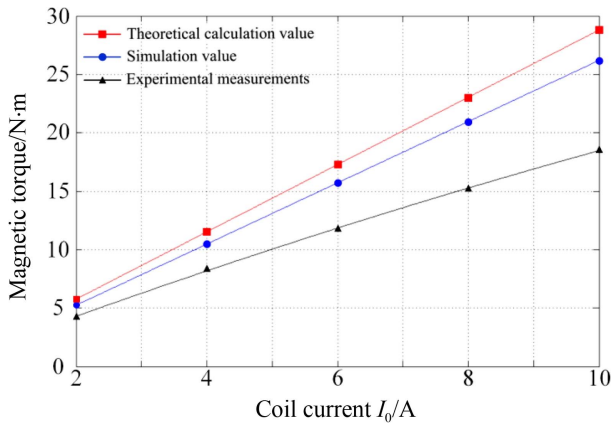

Fig. 16. (Color online) Comparison of Experiment 2 data.

could not be avoided. The increase of coil current led to the increase of relative error between two sets of data under the same magnetic torque device in Fig. 16. The reason was that magnetic field coupling was not considered in the theoretical calculation. Although this phenomenon was noticed in the simulation analysis, but in the actual situation, the coil winding is dense, which led to the heating after power on. The double effect of heating and magnetic coupling was the key to the error. From the overall experimental results, the torque generated by the device was sufficient to meet the requirements of non-extreme wind speed environment under the condition of set parameters.

Under the same high-voltage magnetic field environment, there are some differences between the magnetic torque measured by the above two groups of experiments and the theoretical calculation value and simulation analysis value. Through the analysis of the experimental error, it is found that the error mainly comes from three aspects. In the process of the experiment, the torque was artificially applied to the body because the wind tunnel experiment conditions were not available,. In order to ensure the accuracy of the test results, it was required to maintain the horizontal direction to apply the tension to the body during the experiment, relying only on the naked eye and muscle memory. Only relying on the naked eye and muscle memory to judge will inevitably lead to errors, which is the main source of experimental errors; In the process of magnetic core processing, whether the magnetic core can fully realize its function is closely related to the processing accuracy. Its shape is strictly symmetrical. Particularity, small errors in processing will cause the reduction of magnetic torque. In addition, even if the core gap was filled in the early stage, the magnetic flux leakage can't be avoided; In the process of simulation analysis, the theoretical analysis did not consider that the induced magnetic field generated after the coil was energized would be coupled with the high-voltage magnetic field. At the same time, the heating of the coil also affects the performance of magnetic materials.

6. Conclusion

Aiming at that the current inspection robots were susceptible to wind loads, a magnetic torque device was designed for HVDC inspection robot to improve the stability, operational reliability and safety of the robot under wind loads. According to the proposed theory, a series of simulation and verification work were carried out, and the balance control scheme was studied. Then the live test was carried out in the environment of high voltage transmission line. The experiment proved that the theoretical method was correct. The device which could counteract the wind load moment was made and tested. The experimental results prove that the device could realize the dynamic balance between the ampere force moment which was generated in the HVDC magnetic field and the wind load moment under non-extreme wind speed. Because of the gap between the core and the coil, the magnetic force in the core was not closed, which led to magnetic leakage. But it does not affect the significance of the experiment.

In view of the problems in the prototype experiment, it is necessary to improve the machining accuracy of the magnetic torque device and find a better filling method to avoid magnetic leakage; Overhead transmission lines span a variety of complex terrain, and terrain has a great impact on wind speed. In this paper, the wind moment of the robot was only studied under the specific wind speed conditions. The influence of nonuniform coefficient of wind speed, wind vibration and wind deflection of the conductor was not considered. In the future, it is necessary to make a comprehensive analysis based on the above factors.

References

[1] C. L. Sun, M. Y. Z. Hao, and H. G. Wang, J. Mech. Eng. **46**, 16 (2010).
[2] Z. Hong, G. P. Wu, W. Wang, and P. Hu, Mach. Desg. Manuf. **12**, 197 (2016).
[3] S. Montambault and N. Pouliot, IEEE Intl. Conf. Trans. Distr. Constr. 1211 (2003).
[4] N. Pouliot and S. Montambault, Proc. ICRA 3970 (2008).
[5] S. Montambault and N. Pouliot, 6th. Intl. Conf. Field. Serv. Rbt. 3166 (2007).
[6] K. Toussaint, S. Montambault, and N. Pouliot, J. Field. Robot. **26**, 477 (2009).
[7] N. Pouliot, P. Richard, and S. Montambault, Proc. IEEE/RSJ. Intl. Conf. Intel. Rbt. Sys. 4327 (2012).
[8] P. L. Richard, N. Pouliot, and S. Montambault, IEEE/ASME. Intl. Conf. Adv. Intel. Mech. 1734 (2014).
[9] N. Pouliot, P. L. Richard, and S. Montambault, IEEE Pwr. Nrg. Tech. Sys. J. **2**, 1 (2015).
[10] P. Debenest, M. Guarnieri, and K. Takita, Proc. IEEE Intl. Conf. Rbt. Auto 3978 (2008).
[11] X. L. Zhu, H. G. Wang, L. J. Fang, M. Y. Zhao, and L. D. Wang, J. Rbt. **04**, 385 (2006).
[12] L. D. Wang, H. G. Wang, L. J. Fang, and M. Y. Zhao, J. Rbt. **05**, 451 (2007).
[13] H. Wang, F. Zhang, and Y. Jiang, Proc. IEEE/RSJ Intl. Conf. Intel. Rbt. Sys. 5107 (2010).
[14] W. B. Guo, H. G. Wang, L. Lin, and F. R. Jing, J. Mach. Des. Manu. **10**, 167 (2012).

[15] S. W. Liao, D.C.S. Univ. (2018).
[16] S. S. Fan, D. Yang, D. H. Zhou, and Y. Yan, J. Elec. Meas. Ins. **31**, 1514 (2017).
[17] R. Y. Li, D.C.S. Univ (2017).
[18] Z. Q. Ye, D.C.S. Univ (2017).
[19] F. Lin, Y. H. Huang, J. Li, and C. Luo, S. Pwr. **42**, 52 (2014).
[20] X. J. Xu, L. H. Wu, X. J. Yang, L. Tang, and Y. F. Yang, J. Z. J. Univ. (Eng. Sci.). **10**, 1937 (2016).
[21] X. J. Xu, C. H. Liu, and Y. Yan, J. Magn. **23**, 423 (2018).
[22] X. J. Xu, Y. L. Wang, X. J. Yang, and L. H. Wu, Comp. Simul. **4**, 356 (2017).
[23] D. X. Xie, Z. X. Gao, and C. Z. Yu, Trans. Chn. Electro. Soci. **5**, 32 (2003).